Single-Shot Demodulation for Structured-Illumination Reflectance Imaging in Poultry Quality Assessment

Ashfak Yeafi[a] and Yuzhen Lu[a]

[a]Department of Biosystems and Agricultural Engineering, Michigan State University, East Lansing, MI 48824, United States

ABSTRACT

Structured-illumination reflectance imaging (SIRI) has shown promise for non-destructive poultry meat quality assessment by enhancing subtle reflectance, texture, and surface-geometry information associated with myopathic defects such as woody breast. However, conventional SIRI demodulation approaches require the acquisition of at least three phase-shifted images at each spatial frequency to recover the direct component (DC), amplitude component (AC), and phase-related information. This multi-frame requirement increases imaging time and limits real-time implementation. In this study, a deep learning-based single-shot SIRI demodulation framework was developed to recover demodulated SIRI outputs from only one raw phase-shifted image. A shared-encoder dual-decoder network was designed to simultaneously reconstruct AC, DC, and two-frequency phase-difference ($\Delta\phi$) images. The model was trained using conventionally demodulated images as ground-truth targets, with compound reconstruction losses for AC and DC and a wrapped angular loss for $\Delta\phi$. Experiments were conducted using the public SIRI_PoultryWB dataset, which contains 168 broiler breast fillets, including 72 normal and 96 woody-breast-affected samples. The proposed model achieved SSIM (structural similarity index measure) values of 0.974, 0.988, and 0.941 for AC, DC, and $\Delta\phi$, respectively. For woody breast classification, reconstructed AC+$\Delta\phi$ features achieved 90.21% accuracy using a random forest classifier, close to the 91.32% obtained using traditional three-phase demodulation. The proposed method reduced the required input from three images to one image and achieved 6.7 ms/frame inference latency, demonstrating its potential for faster SIRI-based poultry quality inspection.

Keywords: Structured-illumination, single-shot demodulation, deep learning, poultry quality assessment, woody breast, non-destructive inspection

1. INTRODUCTION

Broiler meat represents one of the most important animal protein sources in the United States (U.S.) and forms a major part of the agricultural economy. In 2025, the U.S. produced 9.40 billion broilers in 2025, corresponding to 62.2 billion pounds of live weight and a production value of approximately $44.6 billion [1]. The high productivity of the modern broiler industry has been achieved through long-term genetic selection for rapid growth, improved feed efficiency, and increased breast meat yield. However, these production gains have also been associated with the prevalence of breast musclular myopathies, particularly white striping and woody breast (WB), which negatively affect meat quality, consumer acceptance, and product value [2–4].

WB is one of the most important quality defects affecting modern broiler breast fillets. WB-affected fillets are typically characterized by abnormal hardness, rigid texture, pale surface regions, and irregular shape profiles. These physical and structural changes reduce product quality and may lead to downgrading, rejection, or diversion of the affected meat to lower-value processed products [2,4,5]. Although the exact biological mechanisms of WB remain to be fully understood, the condition is widely linked to growth-related changes in modern broilers [3,5]. Current WB assessment in poultry processing plants still relies largely on manual hand palpation and visual inspection by trained personnel. Although these approaches are widely used, they are subjective, labor-intensive, contact-based, and prone to operator variability. Manual evaluation is also difficult to standardize for high-speed processing lines, where rapid and consistent inspection is required. Therefore, there is a strong

*Correspondence: luyuzhen@msu.edu

need for non-destructive sensing methods that can provide objective information related to surface appearance, reflectance behavior, texture, and shape-related changes in broiler breast fillets [5–7].

SIRI is an emerging optical imaging technique that projects sinusoidal illumination patterns onto a sample surface and captures the reflected pattern-modulated signal. Through the demodulation of acquired images, SIR can provide three independent sets of outputs, including a DC, which corresponds to uniform information, an AC, which contains structured-illumination-specific contrast, and a phase map that encodes the surface geometry of samples. Compared with conventional uniform illumination imaging, SIRI can enhance subtle surface and subsurface features, improve image contrast, and provide depth-related information by varying the spatial frequency of the projected sinusoidal patterns [8–10]. These characteristics make the imaging technique attractive for food quality inspection tasks where defects are weakly visible, spatially heterogeneous, or not readily captured using conventional uniform illumination-based imaging.

Recent studies have demonstrated the potential of SIRI for poultry meat quality assessment. Olaniyi et al. investigated SIRI combined with deep learning for the assessment of white striping in broiler breast meat and showed that AC image-based features can improve defect detection compared with conventional visual assessment [11]. Cai and Lu further demonstrated that SIRI coupled with surface profilometry was effective for WB assessment in broiler breast fillets, where phase-related information provided more useful cues than intensity images for distinguishing normal and WB-affected samples [6]. These studies highlight the importance of sample texture and geometry-related information captured by AC and phase images of SIRI, respectively, for broiler breast myopathy assessment.

Despite these applications, conventional SIRI demodulation typically requires the acquisition and use of at least three phase-shifted images at each spatial frequency to recover DC, AC, and phase-related information. This multi-frame acquisition requirement increases imaging time, adds synchronization demands between the projector and camera, and thus limits the practical implementation of SIRI for real-time or high-throughput poultry inspection. Reducing the number of required phase-shifted images while preserving diagnostically useful demodulated information is hence an important step toward online SIRI-based poultry quality assessment.

Deep learning has recently shown strong potential for single-shot structured-light reconstruction and phase recovery. In structured-light profilometry, neural networks have been used to estimate phase or three-dimensional (3D) information from a single fringe image, reducing the need for multiple phase-shifted acquisitions [12–14]. However, limited work has been conducted on the single-shot demodulation specifically for SIRI-based food quality inspection, where the goal is not only to reconstruct visually similar demodulated images but also to preserve information useful for downstream defect classification.

Therefore, the overall objective of this study was to develop a deep learning-based single-shot SIRI demodulation framework for poultry quality assessment, specifically by recovering AC, DC, and two-frequency phase-difference ($\Delta\phi$) images from only one phase-shifted SIRI image. A shared-encoder dual-decoder network was designed to reconstruct intensity-related demodulated components (AC and DC) and phase-difference information simultaneously. The reconstructed outputs were compared with conventional three-phase demodulation using quantitative image-quality metrics, and their usefulness was further evaluated through WB classification. By reducing the required number of input images from three to one while preserving useful reflectance and phase-related information, the proposed framework is expected to advance SIRI toward faster and more practical poultry quality inspection.

2. MATERIALS AND METHODS

2.1 Dataset

A publicly available image dataset, i.e., SIRI_PoultryWB dataset [7], was used in this work for developing and evaluating the proposed single-shot demodulation framework for woody breast assessment of broiler meat. The dataset was originally collected using a custom-assembled SIRI system operated inside an enclosed imaging chamber. The imaging platform consisted mainly of a broadband quartz tungsten halogen light source, a digital micromirror device-based projector for sinusoidal pattern projection, a monochromatic camera, and a computer for system control and image acquisition. Three phase-shifted sinusoidal illumination patterns at each spatial frequency were projected onto broiler breast fillets for sample imaging, and the reflected pattern images were

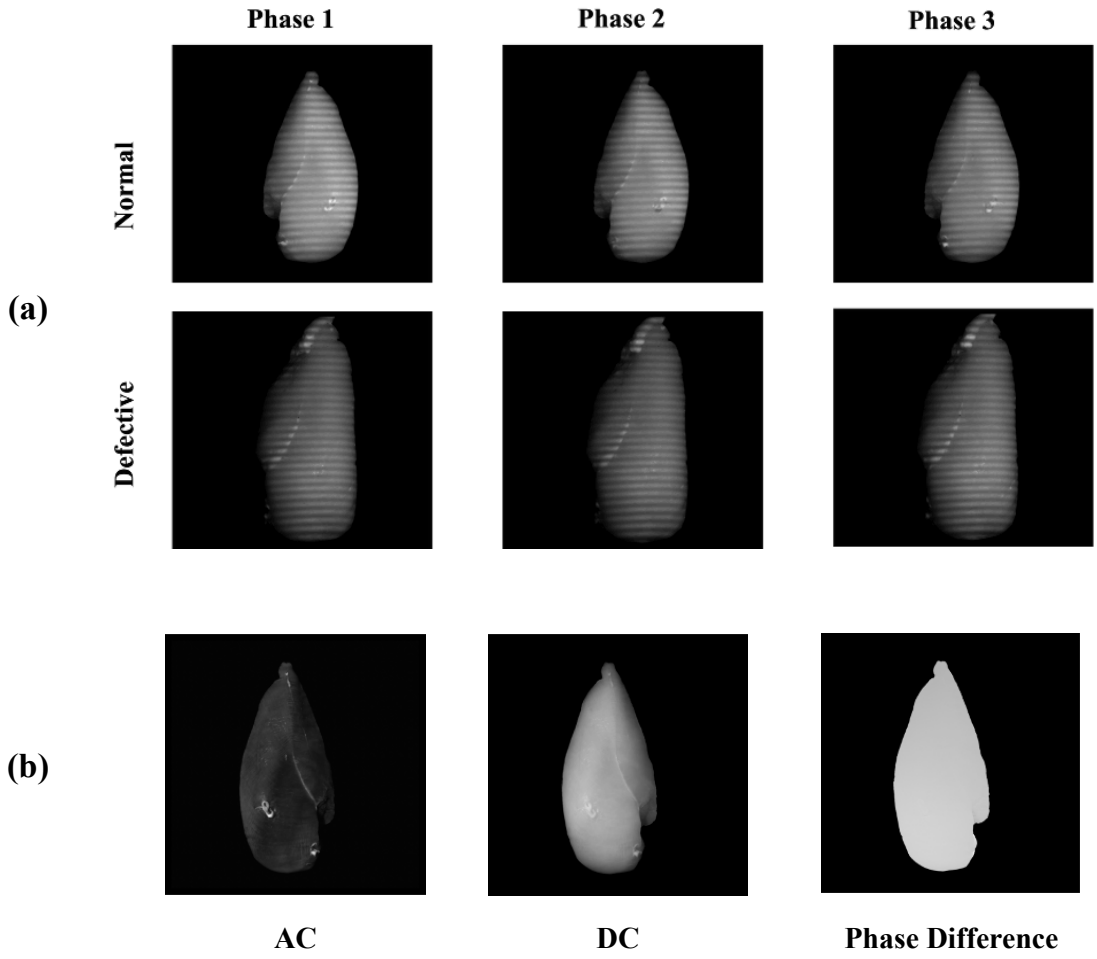

Figure 1. Representative SIRI image samples and ground-truth demodulated targets from the SIRI_PoultryWB dataset. (a) Raw phase-shifted pattern images from normal and woody-breast-affected broiler breast fillets acquired at three phase shifts. (b) Corresponding demodulated target images, including AC, DC, and phase-difference image, used as supervised learning targets for the proposed single-shot demodulation model.

captured by the camera with a resolution of 2048×2048 pixels. A detailed description of the imaging system and acquisition settings is given elsewhere [7].

The dataset contains raw phase-shifted pattern images of 168 broiler breast fillets collected from a commercial poultry processing plant. The samples were labeled by trained personnel based on manual tactile palpation and visual inspection. Among the 168 samples, 72 fillets were labeled as normal, WB-free samples, and 96 fillets were labeled as defective, WB-affected samples. The defective class included 39 moderate and 57 severe WB samples, which were combined into one defective class for binary classification. For each sample, 24 pattern images were acquired from three phase-shifted sinusoidal illumination patterns at eight spatial frequencies (0.015, 0.022, 0.030, 0.040, 0.055, 0.070, 0.090, and 0.150 cycles/mm). Therefore, the complete raw image set contains 4032 phase-shifted pattern images, which were stored in 16-bit grayscale TIFF format.

The dataset is organized into two main image groups: raw phase-shifted pattern images and demodulated images. The raw pattern images contain the three phase-shifted images at each spatial frequency, while the demodulated image folder includes DC, AC, and phase-difference images. For this study, the raw phase-shifted pattern images were used for single-shot input preparation, while the corresponding conventionally demodulated

AC, DC, and phase-difference images were used as supervised learning targets. Representative raw pattern images from normal and woody-breast-affected fillets, together with corresponding demodulated targets, are shown in Figure 1.

2.2 Image preprocessing and input-target preparation

The raw phase-shifted SIRI pattern images and the corresponding demodulated images were used to prepare paired input-target data for supervised learning. Each phase-shifted image was treated as an independent single-shot input during model development, while the corresponding conventionally demodulated outputs served as targets. The corresponding conventionally demodulated AC, DC, and two-frequency phase-difference ($\Delta\phi$) images were used as the target outputs. The use of one raw pattern image as input follows the objective of reducing the conventional three-phase SIRI acquisition requirement to a single-shot demodulation setting.

All input and target images were resized to 512×512 pixels to reduce computational cost while preserving the main spatial structure and fringe-related information needed for demodulation. The image intensities were normalized before model training to improve numerical stability and reduce scale variation among samples. A Gaussian filter was then applied to suppress high-frequency noise and smooth local intensity fluctuations in the images. The same preprocessing settings were applied consistently to the input raw pattern images and the corresponding target images. The dataset was divided at the sample level into training and testing subsets using a 65%/35% split. As shown in Figure 2, the training set contained 46 normal and 62 defective samples, while the testing set contained 26 normal and 34 defective samples.

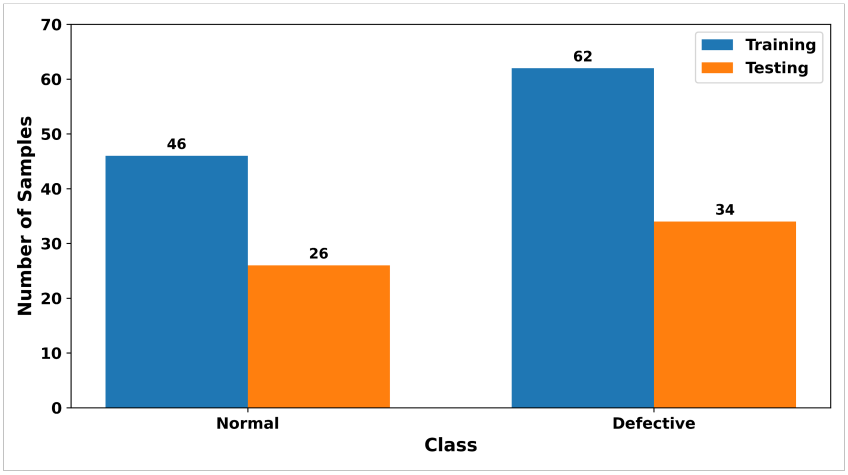

Figure 2. Sample-level training and testing distribution for woody breast classification. The SIRI_PoultryWB dataset was divided using a 65%/35% training-testing split while preserving the normal and defective class groups. The training subset contained 46 normal and 62 defective samples, while the testing subset contained 26 normal and 34 defective samples.

In the proposed framework, the learning task was formulated as a mapping from a single raw phase-shifted SIRI image to multiple demodulated outputs:

$$\hat{Y} = F_\theta(X), \tag{1}$$

where X denotes the selected single phase-shifted image, F_θ represents the proposed deep learning model with trainable parameters θ, and $\hat{Y}$ denotes the predicted demodulated outputs. The target output was defined as follows:

$$Y = \{AC, DC, \Delta\phi\}, \tag{2}$$

where AC represents the AC, DC represents the DC, and $\Delta\phi$ represents the two-frequency phase-difference image. The objective of the model was to learn this single-shot mapping while preserving both intensity-related reflectance information and phase-related geometric information useful for WB assessment.

2.3 Conventional three-phase demodulation

Conventional SIRI demodulation was used to generate the ground-truth target images for supervised model training. For each spatial frequency, the SIRI_PoultryWB dataset provides three raw phase-shifted pattern images acquired with phase offsets of 0, $2\pi/3$, and $4\pi/3$ [7]. Before demodulation, the raw pattern images were filtered using a low-pass Gaussian filter with a 3×3 kernel to suppress image noise.

Let I_1, I_2, and I_3 denote the three filtered phase-shifted reflectance pattern images at the same spatial frequency. The demodulation operations were performed on a pixel-by-pixel basis, with DC, AC, and phase (wrapped) images at a spatial frequency f retrieved as follows:

$$I_{DC} = \frac{1}{3}(I_1 + I_2 + I_3). \tag{3}$$

$$I_{AC} = \frac{\sqrt{2}}{3}\sqrt{(I_1 - I_2)^2 + (I_1 - I_3)^2 + (I_2 - I_3)^2}. \tag{4}$$

$$\varphi_f = \text{atan2}\left[\sqrt{3}(I_1 - I_3), 2I_2 - I_1 - I_3\right], \tag{5}$$

where φ_f denotes the wrapped phase. The DC and AC images characterize intensity-related optical information from the sample, whereas the phase image contains surface-geometry-related information useful for WB assessment [6, 8].

The arctangent operation in Eq. (5) produces phase values wrapped within the interval $-\pi$ to π, resulting in 2π discontinuities in the phase map. Therefore, phase unwrapping was required to recover a continuous absolute phase map. The relationship between the absolute phase Φ_f and the wrapped phase φ_f can be written as:

$$\Phi_f = \varphi_f + 2\pi k, \tag{6}$$

where k is an integer fringe order. In this study, the two-frequency phase-unwrapping method was used to recover the absolute phase [15, 16]. The spatial frequencies of 0.030 cycles/mm and 0.150 cycles/mm were used as the low and high spatial frequencies, respectively. The fringe order k for the high-frequency wrapped phase was determined using:

$$k = \text{Round}\left(\frac{(f_h/f_l)\Phi_l - \varphi_h}{2\pi}\right), \tag{7}$$

where f_h and f_l denote the high and low spatial frequencies, respectively; φ_h is the wrapped phase at the high spatial frequency; and Φ_l is the absolute phase estimated from the low spatial frequency. After obtaining the fringe order k, the high-frequency absolute phase Φ_h was recovered using Eq. (6).

Finally, the phase-difference image was obtained by subtracting an estimated reference phase map from the recovered high-frequency absolute phase:

$$\Delta\phi = \Phi_h - \Phi_{ref}, \tag{8}$$

where Φ_{ref} denotes the estimated reference phase map. The resulting phase-difference image represents surface-profile-related information of the sample. A median filter with a 5×5 kernel was applied to the phase-difference image to reduce noise before subsequent model training and evaluation. In this work, the conventionally demodulated AC, DC, and $\Delta\phi$ images were used as ground-truth targets for training the proposed single-shot demodulation model.

2.4 Proposed single-shot SIRI demodulation framework

The proposed framework was designed to reduce the conventional SIRI demodulation requirement from three phase-shifted pattern images to one raw phase-shifted image. Instead of using all three phase-shifted images for closed-form demodulation, the proposed model learns a direct mapping from a single raw pattern image to the corresponding demodulated outputs. This approach aims to preserve the intensity-related and phase-related information needed for WB assessment while reducing the image acquisition burden.

As shown in Figure 3, the framework consists of three main stages: input preparation, single-shot demodulation, and downstream woody breast classification. In the input preparation stage, one raw phase-shifted SIRI image is selected from each sample and preprocessed. In the demodulation stage, the proposed deep learning model predicts the corresponding AC, DC, and $\Delta\phi$ images. In the final stage, the predicted demodulated outputs are used to prepare feature sets for normal versus WB-affected sample classification.

The single-shot demodulation task was formulated as a multi-output image-to-image regression problem. Given a single raw phase-shifted SIRI image X, the model predicts three demodulated outputs:

$$\{\widehat{AC}, \widehat{DC}, \widehat{\Delta\phi}\} = F_\theta(X), \tag{9}$$

where F_θ represents the proposed neural network with trainable parameters θ, and $\widehat{AC}$, $\widehat{DC}$, and $\widehat{\Delta\phi}$ denote the predicted amplitude component, direct component, and two-frequency phase-difference image, respectively. The corresponding ground-truth targets were obtained from conventional three-phase demodulation and two-frequency phase unwrapping, as described in Eqs. (3)–(8). The use of AC, DC, and $\Delta\phi$ as output targets was

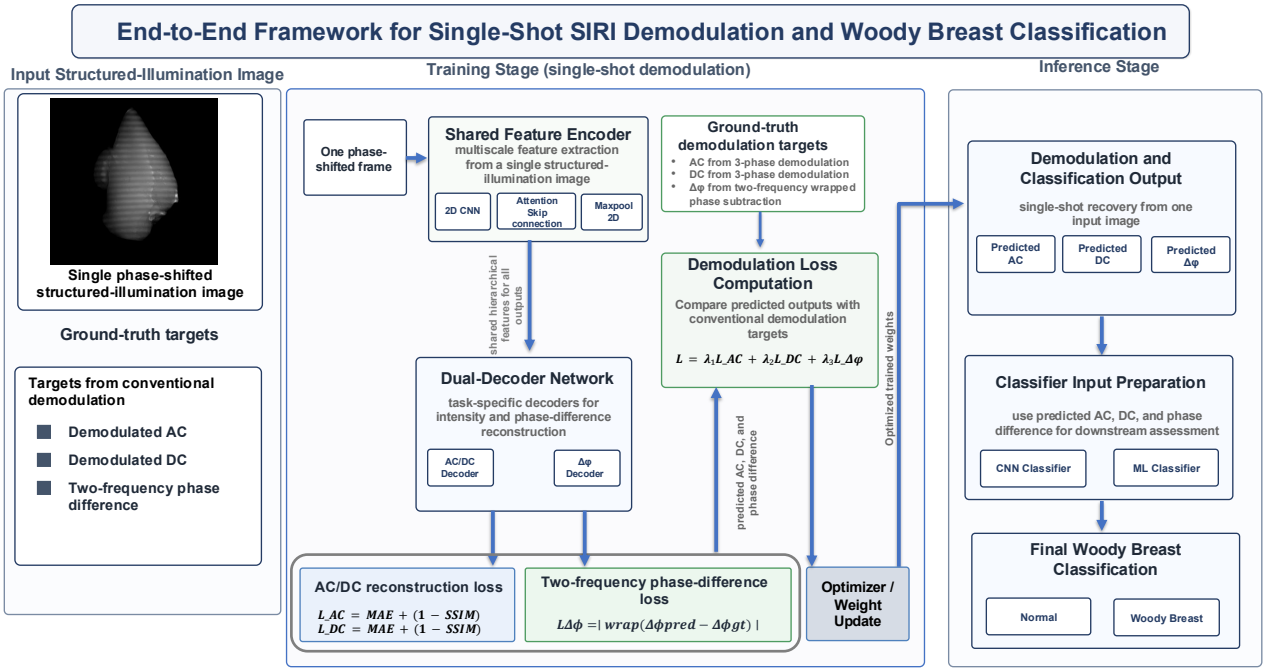

Figure 3. End-to-end framework of the proposed single-shot SIRI demodulation and WB classification method. A single phase-shifted pattern image is used as input to a shared-feature encoder and dual-decoder network to recover AC, DC, and $\Delta\phi$. During training, the predicted outputs are compared with conventional demodulation targets for loss computation and network optimization. During inference, the recovered outputs are used for downstream sample classification.

motivated by their complementary information. The DC image represents uniform reflectance information, the AC image emphasizes structured-illumination contrast related to local texture and subsurface scattering, and the phase-difference image provides geometry-related information associated with surface deformation. Together, these outputs provide a richer representation for WB assessment than a single image component alone.

2.5 Network architecture

A shared-encoder dual-decoder network was developed for single-shot SIRI demodulation. The shared encoder was used to extract multiscale hierarchical features from the input structured-illumination image. Since the input image contains both global sample shape information and local fringe-modulated intensity patterns, the encoder was designed to preserve spatial information across multiple feature scales.

The decoder part of the network contained two branches. The first decoder branch was used for intensity reconstruction and produced the AC and DC images. The second decoder branch was used for phase-related prediction and produced the two-frequency phase-difference image $\Delta\phi$. This dual-decoder design allowed the network to learn both intensity-related and phase-related representations from a shared feature space while allowing each output type to be reconstructed through a task-specific decoding pathway.

Skip connections were included between the encoder and decoder layers to recover spatial details that may be lost during downsampling. Attention modules were also incorporated into the skip pathways to emphasize useful fringe and sample-related features while suppressing less informative background regions [17]. This design was intended to improve reconstruction of fine spatial patterns in AC images and preserve geometry-related structures in the predicted $\Delta\phi$ images.

Figure 4 shows the proposed shared-encoder dual-decoder architecture, including the input raw SIRI image, encoder blocks, attention-guided skip connections, the AC/DC decoder branch, and the $\Delta\phi$ decoder branch.

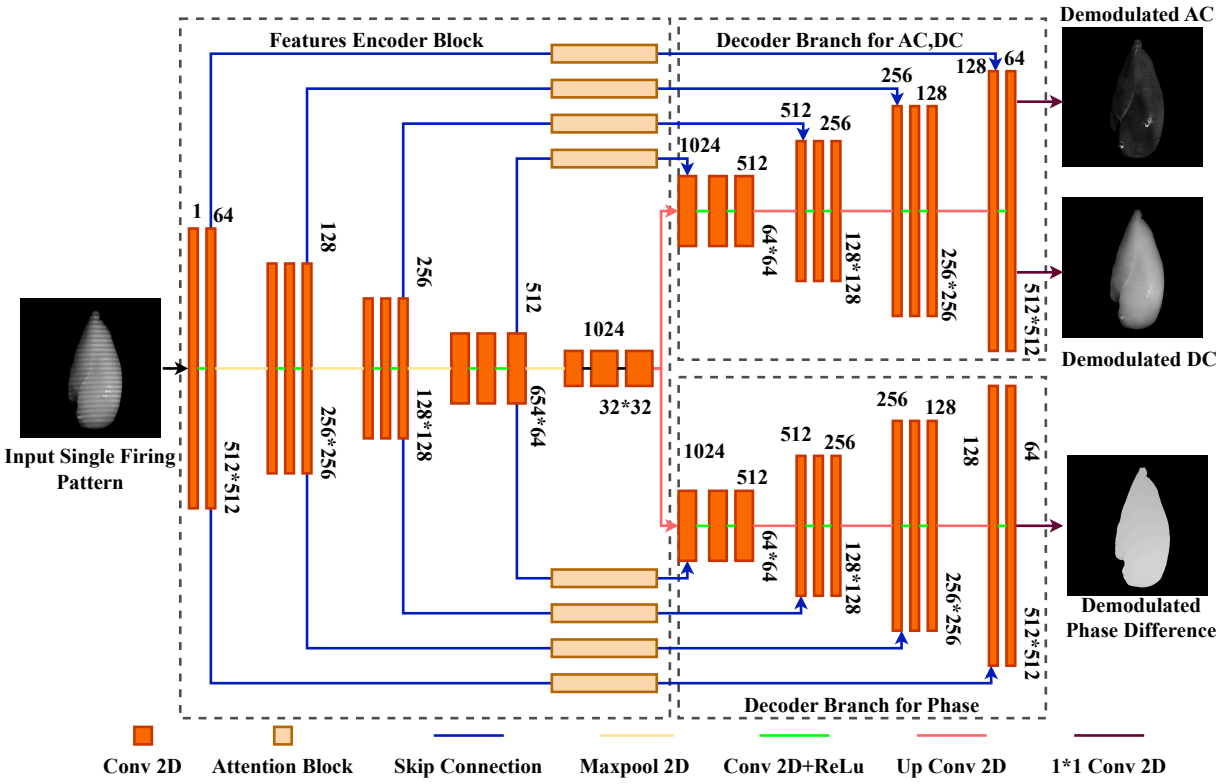

Figure 4. Proposed shared-encoder dual-decoder network for single-shot SIRI demodulation. The shared encoder extracts multiscale features from one phase-shifted raw SIRI image. The intensity decoder reconstructs AC and DC images, while the phase decoder predicts the two-frequency phase-difference image $\Delta\phi$. Attention-guided skip connections are used to preserve fine spatial and fringe-related information.

2.6 Loss functions and training strategy

The proposed single-shot demodulation network was trained in a supervised manner using the conventionally demodulated AC, DC, and $\Delta\phi$ images as ground-truth targets. Since the three output branches represent

different physical information, separate loss terms were defined for intensity reconstruction and phase-difference prediction.

For the AC and DC outputs, a compound reconstruction loss was used by combining mean absolute error (MAE) and structural similarity index measure (SSIM). The MAE term encourages pixel-level intensity accuracy, while the SSIM term helps preserve local structural similarity and spatial contrast between the predicted and ground-truth demodulated images. The AC reconstruction loss was defined as:

$$L_{AC} = MAE(\widehat{AC}, AC) + \left[1 - SSIM(\widehat{AC}, AC)\right], \tag{10}$$

where $\widehat{AC}$ and AC denote the predicted and ground-truth amplitude component images, respectively.

Similarly, the DC reconstruction loss was defined as:

$$L_{DC} = MAE(\widehat{DC}, DC) + \left[1 - SSIM(\widehat{DC}, DC)\right], \tag{11}$$

where $\widehat{DC}$ and DC denote the predicted and ground-truth direct component images, respectively.

For the phase-difference output, a wrapped angular loss was used to account for the periodic nature of phase values. Direct subtraction of phase values can be problematic because phase is wrapped within a limited angular range. Therefore, the angular error was calculated using sine and cosine terms as:

$$e_{\Delta\phi} = \text{atan2}\left[\sin(\widehat{\Delta\phi} - \Delta\phi), \cos(\widehat{\Delta\phi} - \Delta\phi)\right], \tag{12}$$

where $\widehat{\Delta\phi}$ and $\Delta\phi$ denote the predicted and ground-truth phase-difference images, respectively. The phase-difference loss was then calculated as the mean absolute wrapped angular error:

$$L_{\Delta\phi} = \frac{1}{N}\sum_{i=1}^{N} |e_{\Delta\phi,i}|, \tag{13}$$

where N is the total number of pixels in the image.

The total training loss was defined as a weighted sum of the three loss terms:

$$L_{total} = \lambda_1 L_{AC} + \lambda_2 L_{DC} + \lambda_3 L_{\Delta\phi}, \tag{14}$$

where λ_1, λ_2, and λ_3 are weighting coefficients for the AC, DC, and phase-difference losses, respectively. In this study, the loss weights were empirically set to $\lambda_1 = 0.5$, $\lambda_2 = 0.5$, and $\lambda_3 = 0.2$.

The network was implemented using PyTorch and trained using the Adam optimizer. The learning rate was set to 1×10^{-4}, the batch size was set to 8, and the model was trained for 150 epochs. Within the training subset (65% of the total dataset at the sample level), five-fold cross-validation was used during model development to monitor training stability and reduce sensitivity to a single validation partition.

2.7 Performance evaluation

The reconstructed SIRI outputs were evaluated in two stages. First, the quality of the predicted AC, DC, and $\Delta\phi$ images was assessed by comparing them with the corresponding conventionally demodulated ground-truth images. Second, the usefulness of the reconstructed outputs was evaluated through downstream WB classification based supervised modeling.

For reconstruction evaluation, three image-quality metrics were used, including MAE, SSIM, and peak signal-to-noise ratio (PSNR). MAE was used to measure the average pixel-wise difference between the predicted and ground-truth images:

$$MAE = \frac{1}{N}\sum_{i=1}^{N}\left|\hat{Y}_i - Y_i\right|, \tag{15}$$

where $\hat{Y}_i$ and Y_i denote the predicted and ground-truth pixel values at pixel location i, respectively, and N is the total number of pixels. SSIM was used to evaluate structural similarity by considering luminance, contrast, and structural consistency between the predicted and ground-truth outputs. PSNR was calculated as:

$$PSNR = 10\log_{10}\left(\frac{MAX_Y^2}{MSE}\right), \tag{16}$$

where MAX_Y is the maximum possible pixel intensity value after normalization and MSE is the mean squared error between the predicted and ground-truth images. In addition to the three image quality metrics, the processing efficiency of the proposed single-shot framework was computed to assess its potential for online implementation, in comparison with traditional three-phase demodulation.

For downstream sample classification, the reconstructed demodulated outputs were used as feature inputs to distinguish normal fillets from WB-affected fillets. Different feature sets were evaluated, including AC, DC, $\Delta\phi$, and the combined AC+$\Delta\phi$ representation. The AC component was used to represent structured-illumination reflectance contrast, the DC component was used to represent uniform reflectance information, and $\Delta\phi$ was used to represent phase-related surface geometry information. The AC+$\Delta\phi$ feature set was included to evaluate whether reflectance contrast and phase-related geometry provide complementary information for WB classification. Classification performance was evaluated using precision, recall, and accuracy, calculated as follows:

$$Precision = \frac{TP}{TP+FP}, \tag{17}$$

$$Recall = \frac{TP}{TP+FN}, \tag{18}$$

$$Accuracy = \frac{TP+TN}{TP+TN+FP+FN}, \tag{19}$$

where TP, TN, FP, and FN denote true positives, true negatives, false positives, and false negatives, respectively, and WB-affected and normal samples are treated as the positive and negative classes, respectively.

The main comparison was performed between the proposed single-shot demodulation outputs and the traditional three-phase demodulation baseline. For this comparison, the same classifier and evaluation protocol were applied to both sets of features. This allowed the classification performance gap between the single-shot reconstructed outputs and the conventional demodulated outputs to be evaluated directly. Multiple classifiers were compared using the selected feature representations to examine the robustness of the reconstructed SIRI features for WB classification. The evaluated classifiers included random forest (RF), support vector machine (SVM), k-nearest neighbor (KNN), logistic regression (LR), and convolutional neural network (CNN).

3. RESULTS AND DISCUSSION

3.1 Training performance

The proposed single-shot SIRI demodulation network was trained for 150 epochs. The total training time was approximately 3.5 h. As shown in Figure 5, the training and validation losses decreased steadily for AC, DC, and two-frequency phase-difference ($\Delta\phi$) reconstruction. The validation loss curves followed the training loss curves closely, indicating stable convergence and limited overfitting.

Among the three output branches, the DC reconstruction branch showed the lowest final loss. This is reasonable because the DC image represents the average reflectance response and is less affected by fringe modulation and phase discontinuity. In contrast, the $\Delta\phi$ branch showed a relatively higher final loss because phase-difference prediction is more challenging and requires the model to preserve geometry-related information from only one raw phase-shifted pattern image.

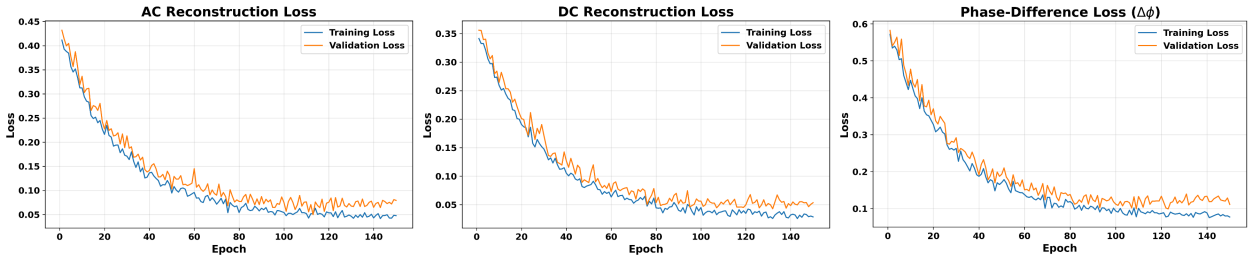

Figure 5. Training and validation loss curves for AC, DC, and two-frequency phase-difference ($\Delta\phi$) reconstruction over 150 epochs. The three curves show stable convergence for AC reconstruction, DC reconstruction, and phase-difference prediction.

3.2 Reconstruction performance

The reconstructed AC, DC, and $\Delta\phi$ images were compared with the corresponding outputs generated by conventional three-phase demodulation. Representative reconstruction results are shown in Figure 6. Visually, the predicted AC and DC images showed strong agreement with the conventional demodulation outputs. The predicted $\Delta\phi$ image also preserved the main sample shape and surface-related structure, although phase-difference reconstruction was more challenging than intensity reconstruction.

Table 1 summarizes the quantitative reconstruction performance. The DC output achieved the best reconstruction quality, with the lowest MAE of 0.018, highest SSIM of 0.988, and PSNR of 33.4 dB. The AC output also showed high reconstruction quality, with an MAE of 0.021, SSIM of 0.974, and PSNR of 31.8 dB. The $\Delta\phi$ output had a higher MAE of 0.067 and lower PSNR of 29.2 dB compared with AC and DC, but still achieved an SSIM of 0.941. This indicates that the proposed model preserved the main structural information in the phase-difference image.

Table 1. Quantitative reconstruction performance of the proposed single-shot SIRI demodulation model.

Output	MAE	SSIM	PSNR (dB)
AC	0.021	0.974	31.8
DC	0.018	0.988	33.4
$\Delta\phi$	0.067	0.941	29.2

These results suggest that a single raw phase-shifted SIRI image contains sufficient information for recovering useful demodulated representations. The higher reconstruction performance of DC can be attributed to its smoother intensity distribution, while AC reconstruction requires preserving fringe-related contrast and local textural variations. The relatively lower performance of $\Delta\phi$ is expected because phase-difference images are related to surface geometry and are normally derived from multiple phase-shifted images and two spatial frequencies.

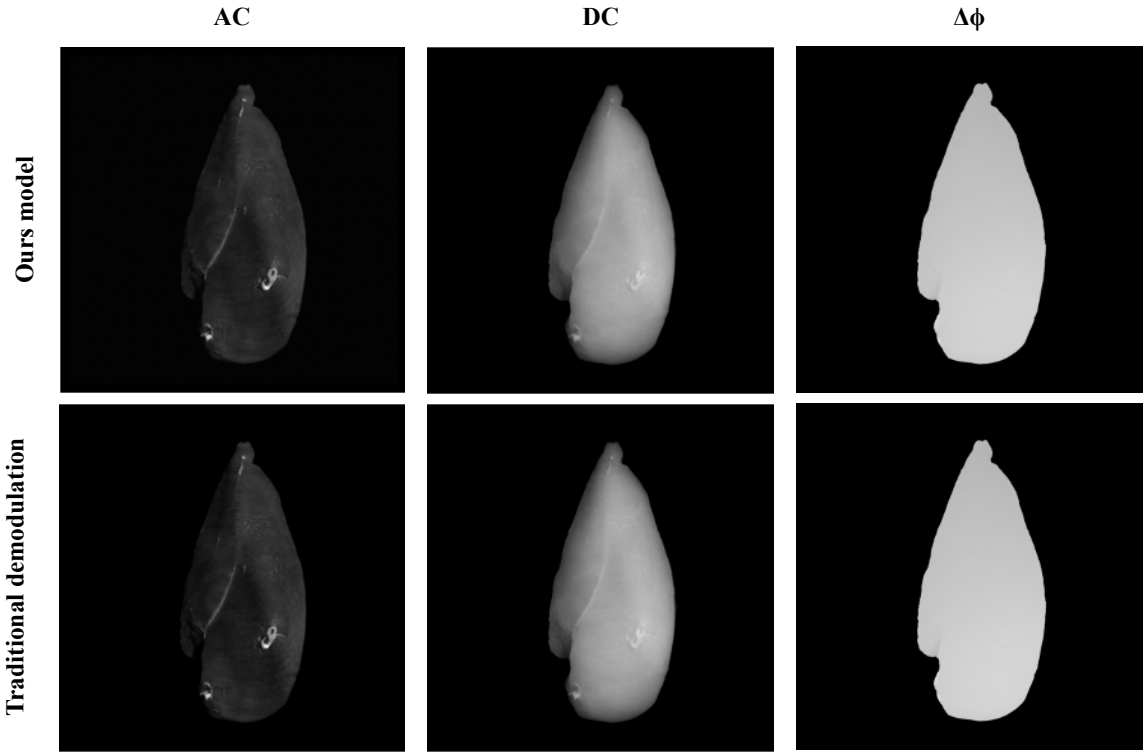

Figure 6. Representative reconstruction results from the proposed single-shot SIRI demodulation model. Predicted AC, DC, and $\Delta\phi$ images are compared with the corresponding conventional three-phase demodulation outputs.

3.3 Sample classification using reconstructed SIRI outputs

To evaluate whether the reconstructed SIRI outputs preserved diagnostically useful information, sample classification was performed using AC, DC, $\Delta\phi$, and AC+$\Delta\phi$ feature sets. The classification performance of the proposed single-shot outputs was compared with the traditional three-phase demodulation baseline using the same RF classifier. The results are summarized in Table 2.

Table 2. Woody breast classification performance using reconstructed SIRI features and traditional three-phase demodulation features.

Feature set	Proposed single-shot model			Traditional demodulation		
	PRE (%)	Recall (%)	Accuracy (%)	PRE (%)	Recall (%)	Accuracy (%)
AC	84.71	85.02	83.96	85.88	86.14	85.54
DC	81.43	82.05	80.74	83.57	84.12	83.21
$\Delta\phi$	87.16	87.84	86.91	88.76	89.03	88.42
AC+$\Delta\phi$	90.28	90.94	90.21	91.68	92.03	91.32

Among the individual feature sets, $\Delta\phi$ achieved better classification performance than AC and DC, reaching 86.91% accuracy using the proposed single-shot outputs. This suggests that phase-related surface geometry information is important for distinguishing normal and WB-affected fillets. DC produced the lowest classification accuracy, indicating that uniform reflectance information alone was less discriminative for this task.

The combined AC+$\Delta\phi$ feature set achieved the best performance for both the proposed single-shot model and the traditional demodulation baseline. Using reconstructed single-shot outputs, AC+$\Delta\phi$ achieved 90.28% precision, 90.94% recall, and 90.21% accuracy. The traditional demodulation baseline achieved 91.68% precision, 92.03% recall, and 91.32% accuracy using the same feature combination. The accuracy difference between

the proposed model and the traditional baseline was only 1.11 percentage points, indicating that the single-shot demodulation model preserved most of the classification-relevant information while reducing the image requirement from three phase-shifted images to one.

3.4 Comparison of different classifiers

The AC+$\Delta\phi$ feature set was further evaluated using different classifiers. As shown in Figure 7, the CNN achieved the best overall performance, with 92.18% precision, 92.46% recall, and 92.31% accuracy. RF also performed strongly, reaching 90.28% precision, 90.94% recall, and 90.21% accuracy. SVM and LR showed moderate classification performance, while KNN achieved the lowest accuracy of 86.74%. The lower KNN performance suggests that the reconstructed feature space may not be optimally separated using simple distance-based decision rules.

Overall, the classifier comparison indicates that the reconstructed AC+$\Delta\phi$ representation contains useful information for WB classification. The strong performance of CNN suggests that learning spatial patterns directly from the reconstructed SIRI outputs may provide additional discriminative power beyond conventional handcrafted or shallow machine-learning features.

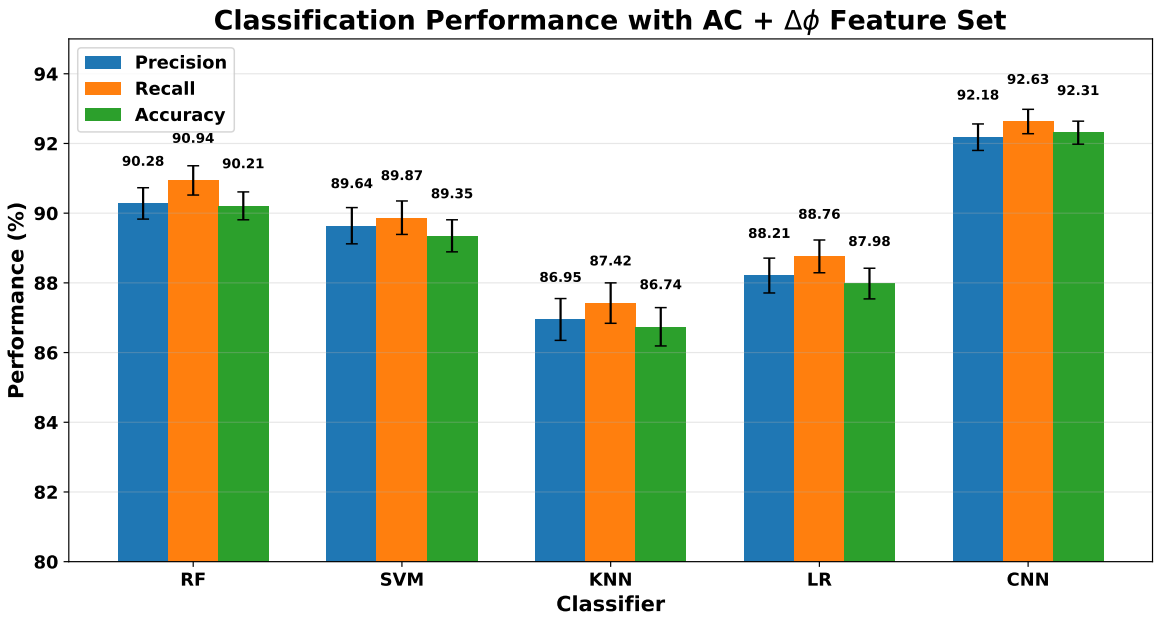

Figure 7. Comparison of different classifiers using the reconstructed AC+$\Delta\phi$ feature set. Precision, recall, and accuracy are reported for random forest (RF), support vector machine (SVM), k-nearest neighbor (KNN), logistic regression (LR), and convolutional neural network (CNN) classifiers.

3.5 Acquisition and processing efficiency

Traditional three-phase demodulation requires three phase-shifted images at each spatial frequency, whereas the proposed method requires only one raw phase-shifted image as input. This reduces the number of required input frames by approximately 66.7%. Table 3 compares the input-frame requirement and processing time between conventional three-phase demodulation and the proposed single-shot demodulation model. The traditional method requires three phase-shifted input images and an exposure-plus-processing time of more than 1500 ms (based on the camera exposure of 500 ms for image acquisition in [6]). In contrast, the proposed method requires one input image, with 500 ms exposure time and 6.7 ms model inference time. This indicates that the proposed framework can substantially reduce imaging time while maintaining comparable demodulation quality and sample classification performance.

The reduction from three frames to one frame represents an important step toward future online poultry inspection because high-throughput processing environments require rapid and synchronized image acquisition.

Table 3. Comparison of acquisition and processing efficiency between traditional demodulation and the proposed single-shot model.

Method	Required input frames	Exposure + processing time (ms)
Traditional three-phase demodulation	3 phase-shifted images	1500+
Proposed single-shot demodulation	1 phase-shifted image	500 + 6.7

Although the current dataset was acquired from stationary samples, these results suggest that proposed single-shot demodulation could help move SIRI-based poultry quality assessment closer to real-time implementation. Future work should evaluate the approach using larger datasets, additional myopathic conditions, and imaging configurations designed for moving samples.

4. CONCLUSION

This study developed a deep learning-based single-shot SIRI demodulation framework for poultry woody breast assessment. Instead of relying on the conventional three-phase demodulation process, the proposed method used only one raw phase-shifted SIRI image to recover AC, DC, and two-frequency phase-difference ($\Delta\phi$) image. A shared-encoder dual-decoder network was designed to learn both intensity-related and phase-related demodulation outputs from a single structured-illumination image. The proposed model achieved strong agreement with conventional three-phase demodulation. Among the reconstructed outputs, DC showed the highest reconstruction quality, while AC and $\Delta\phi$ also preserved useful structural and reflectance-related information. Quantitatively, the model achieved SSIM values of 0.974, 0.988, and 0.941 for AC, DC, and $\Delta\phi$, respectively. These results indicate that a single phase-shifted raw SIRI image contains sufficient information to recover useful demodulated representations for poultry quality assessment. In the further downstream WB classification, among the tested feature sets, AC+$\Delta\phi$ achieved the best classification performance, confirming that the reflectance contrast and phase-related surface geometry provide complementary information for identifying WB-affected fillets. Using the reconstructed AC+$\Delta\phi$ features, the proposed single-shot model achieved 90.21% classification accuracy with a random forest classifier, which was close to the 91.32% accuracy obtained using traditional three-phase demodulation features. The proposed method reduced the required number of input images from three phase-shifted images to one phase-shifted image; under the current implementation, it achieved an inference time of 6.7 ms/frame for image demodulation. Future work will focus on expanding the dataset, evaluating additional poultry defects, improving phase-difference reconstruction, and testing the proposed framework under online imaging conditions for moving samples.

ACKNOWLEDGMENTS

This work was supported by the Michigan State University Discretionary Funding Initiative. The authors acknowledge the creators of the SIRI_PoultryWB dataset and Miller Poultry, Orland, Indiana, for providing the chicken samples used in the original dataset.

REFERENCES

[1] USDA National Agricultural Statistics Service, "Poultry – production and value: 2025 summary," tech. rep., United States Department of Agriculture, National Agricultural Statistics Service (Apr. 2026).

[2] Kuttappan, V., Hargis, B., and Owens, C., "White striping and woody breast myopathies in the modern poultry industry: a review," *Poultry Science* **95**(11), 2724–2733 (2016).

[3] Huang, X. and Ahn, D. U., "The incidence of muscle abnormalities in broiler breast meat–a review," *Korean journal for food science of animal resources* **38**(5), 835 (2018).

[4] Barbut, S., "Recent myopathies in broiler's breast meat fillets," *World's poultry science journal* **75**(4), 559–582 (2019).

[5] Caldas-Cueva, J. P. and Owens, C. M., "A review on the woody breast condition, detection methods, and product utilization in the contemporary poultry industry," *Journal of Animal Science* **98**(8), skaa207 (2020).

[6] Cai, J. and Lu, Y., "Assessment of woody breast in broiler breast fillets using structured-illumination reflectance imaging coupled with surface profilometry," *Journal of Food Engineering* **391**, 112459 (2025).

[7] Lu, Y. and Sardari, H., "A structured-illumination reflectance imaging dataset for woody breast assessment of broiler meat," *Data in Brief* **60**, 111612 (2025).

[8] Lu, Y. and Lu, R., "Structured-illumination reflectance imaging for the detection of defects in fruit: Analysis of resolution, contrast and depth-resolving features," *Biosystems engineering* **180**, 1–15 (2019).

[9] Li, R., Lu, Y., and Lu, R., "Structured illumination reflectance imaging for enhanced detection of subsurface tissue bruising in apples," *Transactions of the ASABE* **61**(3), 809–819 (2018).

[10] Sun, Y., Lu, R., Lu, Y., Tu, K., and Pan, L., "Detection of early decay in peaches by structured-illumination reflectance imaging," *Postharvest Biology and Technology* **151**, 68–78 (2019).

[11] Olaniyi, E., Lu, Y., Sukumaran, A. T., Jarvis, T., and Rowe, C., "Non-destructive assessment of white striping in broiler breast meat using structured-illumination reflectance imaging with deep learning," *Journal of the ASABE* **66**(6), 1437–1447 (2023).

[12] Van der Jeught, S. and Dirckx, J. J., "Deep neural networks for single shot structured light profilometry," *Optics express* **27**(12), 17091–17101 (2019).

[13] Nguyen, A.-H., Ly, K. L., Lam, V. K., and Wang, Z., "Generalized fringe-to-phase framework for single-shot 3d reconstruction integrating structured light with deep learning," *Sensors* **23**(9), 4209 (2023).

[14] Song, Z., Xue, J., Lu, W., Jia, R., Xu, Z., and Yu, C., "Se-fscnet: full-scale connection network for single-shot phase demodulation," *Optics Express* **32**(9), 15295–15314 (2024).

[15] Huntley, J. M. and Saldner, H., "Temporal phase-unwrapping algorithm for automated interferogram analysis," *Applied optics* **32**(17), 3047–3052 (1993).

[16] Zhao, H., Chen, W., and Tan, Y., "Phase-unwrapping algorithm for the measurement of three-dimensional object shapes," *Applied optics* **33**(20), 4497–4500 (1994).

[17] Yeafi, A. and Sarker, L., "Adtnet: Attention-guided u-net with dynamic cnn and transformers for skin cancer detection," in [*2024 13th International Conference on Electrical and Computer Engineering (ICECE)*], 679–684, IEEE (2024).